



Hot deformation behavior and processing maps of an equiatomic MoNbHfZrTi refractory high entropy alloy

Fuyu Dong^a, Ye Yuan^a, Weidong Li^b, Yue Zhang^{a,*}, Peter K. Liaw^b, Xiaoguang Yuan^a, Hongjun Huang^a

^a School of Materials Science and Engineering, Shenyang University of Technology, Shenyang, 110870, China

^b The Department of Materials Science and Engineering, University of Tennessee, Knoxville, TN, USA

ARTICLE INFO

Keywords:

Refractory high-entropy alloy
Deformation mechanism
Flow-stress analysis
Dynamic recrystallization
Microstructure
Processing maps

ABSTRACT

The high-temperature deformation mechanisms and processing maps of an equiatomic body-centered-cubic (BCC) structured MoNbHfZrTi refractory high-entropy alloy (RHEA) were studied over the temperatures ranging from 1100 to 1250 °C and different strain rates varying from 10^{-3} to 0.5 s^{-1} . Flow-stress analyses were performed, using an Arrhenius type relation. The activation energy (Q) for high-temperature deformation was calculated as 326.1 kJ/mol, and the related strain rate sensitivity (m), the power dissipation (η), and instability parameter (ξ) were also derived. The optimal processing area was at 1110–1170 °C and 10^{-3} – $10^{-2.5} \text{ s}^{-1}$, with only one unstable region. Detailed microstructural analyses including the surface cracks were carried out in both stable and unstable regions to confirm the derived. Dynamically recrystallized grains with necklace morphologies were observed along grain boundaries and shear bands, indicating that softening was caused by dynamic recrystallization (DRX). The size and proportion of the DRX grains increase with the strain rate decreasing and the temperature increasing.

1. Introduction

High-entropy alloys (HEAs) are a new family of solid-solution alloys made of five or more multi-principal elements, with each constituent element having a concentration from 5 to 35 atomic percent (at.%) [1–4]. Following the discovery of the first HEAs, several sub-categories have been developed, including eutectic high-entropy alloys [5–7], refractory high-entropy alloys (RHEAs) [8], and light-weight high entropy alloys [9–11], etc. RHEAs, first proposed by Senkov et al. [8], are a family of HEAs consisting predominantly of refractory elements of high melting points and featuring single body-centered-cubic (BCC) structures. They do not only possess typical characteristics of HEAs, but also have excellent mechanical properties at elevated temperatures. Recently, a series of new RHEAs with excellent wear resistance, oxidation resistance, strength and thermal stability at both ambient and elevated temperatures have been designed and reported [12–21]. A few examples are given as follows. The single-phase WNbMoTa and WNbMoTaV RHEAs achieved compressive yield strengths of 405 and 477 MPa, respectively at 1600 °C [22]. The HfNbTaTiZr alloy has been reported to exhibit a total strain of 0.5 under room-temperature

compressions [23]. The MoNbHfZrTi RHEA designed by Guo et al. [24] has a yield strength of 397 MPa at 1100 °C, and possesses good thermal stability. Besides, the relationship between compressive strengths and testing temperatures in RHEAs and two Ni-based superalloys have been comparatively studied [4]. Given many high-temperature properties of RHEAs, they have been considered as promising replacement materials of traditional high-temperature alloys [25].

Studies have been conducted to analyze the microstructural evolution, flow behaviors, and deformation mechanism of several HEAs [26–29]. At present, the hot deformation behavior of high entropy alloys is mainly around Face-centered cubic (FCC) alloys, such as FeCoNiCrMn [26,28,30]. Compared with these high-entropy alloys, the research on the hot deformation of RHEAs is still rare, although Senkov [23], Guo [24,31], and Eteti [32] have done some in this area. Among the work done already in this area, Senkov, and Eteti mainly focused on the HfNbTaTiZr RHEA, whereas Guo focused on the TiZrHfNbMo RHEA, which is also the material used in our work. The main purpose of the previous work is to understand the hot deformation behavior in order to regulate the microstructures, but the hot workability of RHEAs is rarely involved. Guo performed thermal-simulation tests on the TiZrHfNbMo

* Corresponding author.

E-mail address: yuezhang@sut.edu.cn (Y. Zhang).

<https://doi.org/10.1016/j.intermet.2020.106921>

Received 17 June 2020; Received in revised form 23 July 2020; Accepted 24 July 2020

Available online 11 September 2020

0966-9795/© 2020 Elsevier Ltd. All rights reserved.

RHEA, but did not establish a constitutive relationship connecting the flow stress, deformation temperature, strain rate, and strain. Despite it is known that hot processing can play a vital role in affecting the properties of high-temperature alloys, the studies of this topic in HEAs are very rare [29,33–35]. Therefore, a further study on the hot processing of RHEAs is necessary and useful to mature the high-temperature applications of these alloys.

In this work, the stress-strain analyses of the MoNbHfZrTi RHEAs at temperatures ranging from 1100 to 1250 °C and strain rates varying from 10^{-3} to 0.5 s^{-1} were measured by the thermo-simulation machine (Gleeble 3500). Based on the measured peak stresses, a rheological model was established and a hot-processing map for the MoNbHfZrTi RHEA was acquired. The findings do not only provide theoretical foundations to the processing of the MoNbHfZrTi RHEAs, but also practically assist in locating appropriate processing conditions. The accuracy of the thermal-processing map was verified by analyzing the surface cracking of the samples, as well as the microstructure evolution of the destabilized and well-processed regions. The microstructural evolution and the change in deformation mechanisms of the material at various temperatures and strain rates were also examined.

2. Experimental procedures

Equiatomic MoNbHfZrTi RHEA ingots were produced by vacuum arc melting, using the raw materials of >99.9 wt percent (wt.%) purity. The phases in the MoNbHfZrTi RHEA samples before and after hot compressions were analyzed by an X-ray diffractometer (XRD). The samples were cut into cylinders ($\Phi 6 \times 9 \text{ mm}$) using an electric discharge wire-cutting machine, following which the compression tests were executed on a Gleeble 3500 thermo-simulation machine (Dynamic Systems Inc., Poestenkill, NY, USA). Cylindrical specimens were ground with sandpapers of different grits and then welded with a platinum-iridium electrode to allow temperature measurements. A sample was separated from the indenter by a Ta bract to reduce the surface friction and produce the even stress. Compression tests were conducted at various temperatures (1,100, 1,150, 1,200, and 1250 °C) and different strain rates (0.001 , 0.01 , 0.1 , and 0.5 s^{-1}) till a 60% reduction in the sample height is achieved. With a fixed heating rate of 10 °C/s , the samples were heated up to the set temperatures and then lasted for 180s to ensure the temperature uniformity. At the end of experiments, the samples were water quenched immediately to capture and observe their high temperature microstructures. All experiments were carried out in a chamber filled with the pressurized argon to minimize sample oxidation.

For microstructural observations, the hot-deformation samples were cut along the compression direction, and the surfaces were ground with sandpapers and electropolished to a mirror finish. Electropolishing was carried out in an electrolyte composed of 6-vol percent (vol%) perchloric acid, 35-vol % n-butanol and 59-vol % methanol. Liquid nitrogen was used as a cooling medium in the electrolysis process, and the current was held constant at 2.5 A. Electron back-scattering diffraction (EBSD) was used to observe the microstructure of the hotly-compressed samples at a scan step size of $0.3 \mu\text{m}$. The Channel 5 software was used to process the EBSD data from all specimens, the inverse pole figure (IPF) maps, grain boundary (GB) maps, and the local misorientation images were obtained.

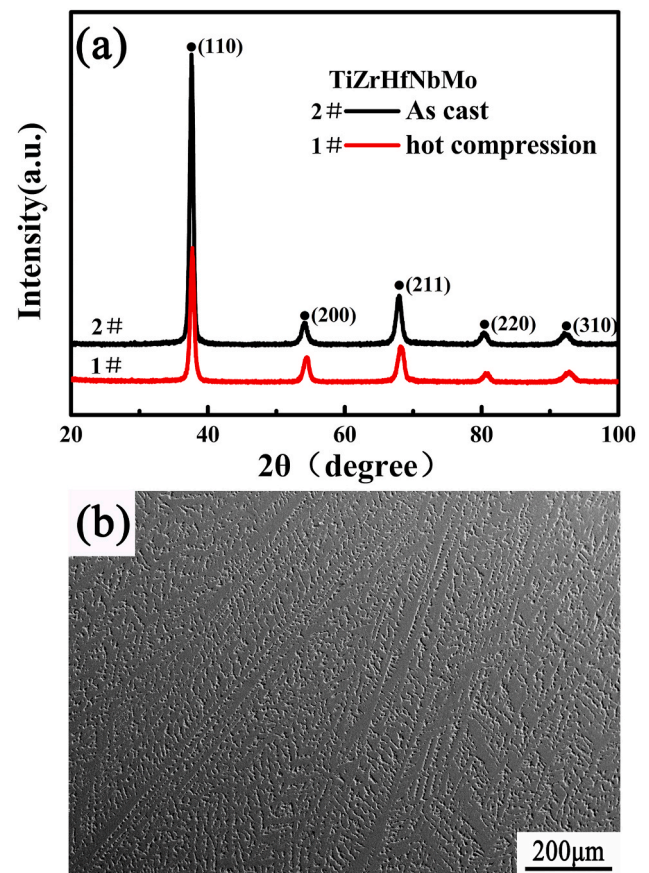


Fig. 1. (a) XRD pattern of the as-cast equiatomic MoNbHfZrTi alloy, (b) SEM image of the as-cast alloy.

3. Results

3.1. Starting material

The XRD patterns showed that the material did not undergo any phase change after hot deformation but remained a single BCC structure (Fig. 1a). The alloy microstructure of as-cast condition was observed by the scanning electron microscope (SEM, Fig. 1b), indicating a dendritic structure. The elemental maps given in Fig. 2 showed that compositional segregation takes place in the material. Specifically, Nb and Mo are rich in dendrites; Zr and Ti are rich in the inter-dendritic regions; and Hf distributes uniformly throughout the domain studied.

3.2. Stress-strain behaviors

The stress-strain curves of the equiatomic MoNbHfZrTi RHEA samples obtained under various deformation conditions all show similar shapes, as evidenced in Fig. 3. As the strain increases, the flow curves show work hardening in the early stages, and then the flow stresses continue to soften. This characteristic is typically recognized as the dynamic recrystallization (DRX) of the alloy deformed in hot compression [36–40]. In the initial stage of deformation, the increased dislocation density in the alloy and the formation of numerous subgrain boundaries cause the accumulation of a high density of dislocations. At this point, work hardening causes a sharp rise in the stress. With further

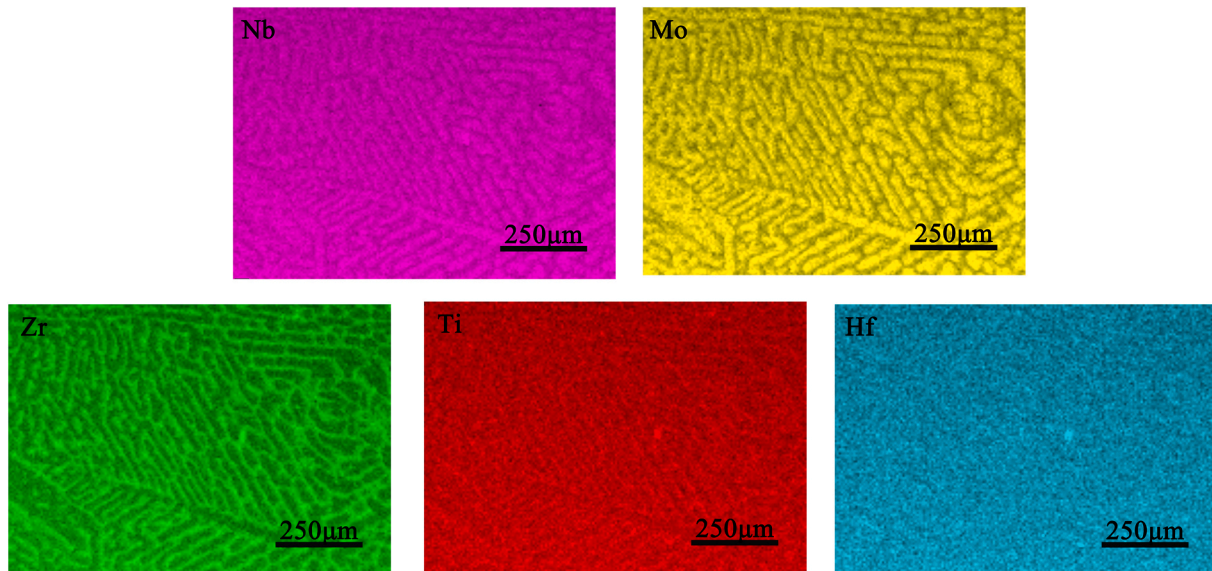


Fig. 2. Elemental maps of the as-cast alloy.

increase in the strain, constant softening is due to DRX, which will be examined through microstructural observations in the later part. Furthermore, the decrease of the peak stress was observed with increasing temperatures and decreasing strain rates, as illustrated in Fig. 3e.

3.3. Constitutive law construction

The high-temperature deformation of metals is a thermal-activation process, and the influence of deformation temperature (T), strain, and strain rate on the flow stress is usually described by the widely-used Arrhenius-type relation [41]. The constitutive equation can be used for predicting the hot deformation ability and microstructural evolution of materials. The Arrhenius-type power law preceded by a hyperbolic function of stress is given as

$$\dot{\varepsilon} = A_1 \sigma^{n_1} \quad (\alpha\sigma \leq 0.8) \quad (1)$$

$$\dot{\varepsilon} = A_2 \exp(\beta\sigma) \quad (\alpha\sigma \geq 1.2) \quad (2)$$

$$\dot{\varepsilon} = A [\sinh(\alpha\sigma)]^n \exp\left(-\frac{Q}{RT}\right) \quad (\text{for all } \sigma) \quad (3)$$

where $\dot{\varepsilon}$ is the strain rate, A , A_1 , A_2 , α , β material constants, σ the flow stress (MPa), n , n_1 the stress exponents, Q the apparent activation energy for hot deformation (kJ/mol), R the gas constant, and T the deformation temperature (K). Peak stresses are extracted from Fig. 3, and the values of n_1 and β are calculated by taking the logarithm and derivation of Eqs. (1) and (2), respectively, i.e.,

$$\ln \dot{\varepsilon} = \ln A_1 + n_1 \ln \sigma \quad (4)$$

$$\ln \dot{\varepsilon} = \ln A_2 + \beta \sigma \quad (5)$$

For calculating the values of n_1 and β , the $\ln(\dot{\varepsilon})$ vs. $\ln(\sigma)$ and $\ln(\dot{\varepsilon})$ vs. σ are plotted in Fig. 4a and b, respectively. The linear relationships obtained for various temperatures are similar, and the calculations yield $n_1 = 3.96216$, $\beta = 0.01216$, and $\alpha = \beta/n_1 = 0.00316$.

The activation energy (Q) for high-temperature deformation was obtained according to the following equation derived from Equation (3)

$$Q = R \left[\frac{\partial \ln(\dot{\varepsilon})}{\partial \ln \sinh(\alpha\sigma)} \right]_T \left[\frac{\partial \ln \sinh(\alpha\sigma)}{\partial \frac{1}{T}} \right] \quad (6)$$

For calculating the activation energy (Q), $\ln(\dot{\varepsilon})$ vs. $\ln \sinh(\alpha\sigma)$ and $\ln \sinh(\alpha\sigma)$ vs. $1/T$ are plotted in Fig. 5a and b, respectively. Linear relationships obtained are nearly parallel. The average slopes from Fig. 5a and b are 2.88 and 1.36, respectively. The computed Q is determined to be 326.1 kJ/mol.

The Zener-Hollomon parameter [42] is widely accepted for characterizing the relationship between the temperature and strain rate simultaneously. The temperature-compensated strain rate, Z parameter was given as

$$Z = \dot{\varepsilon} \exp\left(\frac{Q}{RT}\right) = A [\sinh(\alpha\sigma)]^n \quad (7)$$

Based on Equation (7), $\ln Z$ vs. $\ln \sinh(\alpha\sigma)$ relations obtained during the tests under various temperatures and strain rates are plotted in Fig. 6. From the linear-regression analysis, the relationship between $\ln Z$ and $\ln \sinh(\alpha\sigma)$ was obtained as

$$\ln Z = 22.611 + 2.85 \ln \sinh(\alpha\sigma) \quad (8)$$

Substituting the calculated value of Q , α , A , n , = (326.1 kJ/mol, $\alpha = \beta/n_1 = 0.00316$, 6.60×10^9 , and 2.88232) into Equation (3), the constitutive equation of the refractory high-entropy alloy is given as

$$\dot{\varepsilon} = 6.60 \times 10^9 [\sinh(0.00316\sigma)]^{2.88232} \exp\left(-\frac{326.111}{RT}\right) \quad (9)$$

3.4. Hot-processing map construction

The dynamic material model (DMM) was first established by Prasad et al. [43] and then improved by Rao and Murty [44,45]. DMM analyzes the structural evolution from the perspective of energy conversion in hot deformation. The input energy to the work piece during deformation consists of two sections: dissipative quantity (G) and dissipative covariate quantity (J). The dissipative quantity (G) is mostly converted into the thermal energy, and the dissipative covariate quantity (J) is the energy consumed during the evolution of the material microstructure. The ratio of the two energy quantities can be expressed as the strain-rate-sensitivity index (m) [46]. In order to describe the proportion of energy used for the evolution of the microstructure, the power

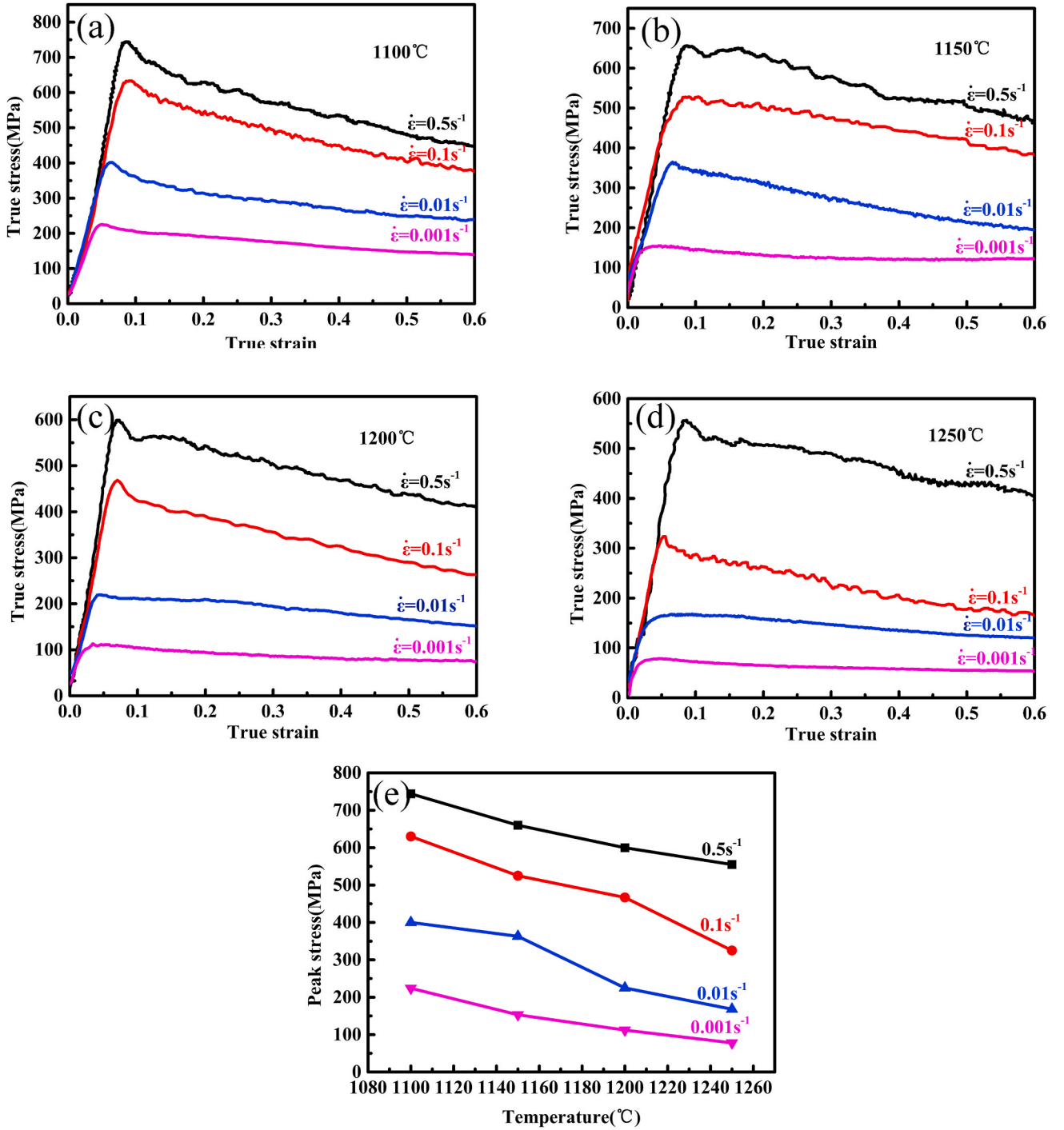


Fig. 3. The true stress-strain curves for the MoNbHfZrTi RHEA obtained from the uniaxial compression tests at various strain rates: (a) 1100 °C, (b) 1150 °C, (c) 1200 °C, (d) 1250 °C and (e) Effects of deformation temperature and strain rate on the peak stress.

dissipation factor η is introduced. When the material is in the ideal linear dissipation state, the strain rate sensitivity exponent m is equal to 1, and then the dissipation coordination reaches the maximum value J_{\max} . The power dissipation factor, η , of the material is obtained through dividing the actual dissipation coefficient (J) by the maximum dissipation coordination (J_{\max}) of the material.

$$\eta = \frac{J}{J_{\max}} = \frac{2m}{m+1} \quad (10)$$

The material instability is judged, using the material-flow instability criterion proposed by Prasad [47].

$$\xi(\dot{\epsilon}) = \frac{\partial \ln[m/(m+1)]}{\partial \ln \dot{\epsilon}} + m < 0 \quad (11)$$

According to the criterion, that area having $\xi < 0$ is the instability zone. The value of m can be obtained from $\log \sigma$ and $\log \dot{\epsilon}$, while $\log \sigma$ and $\log \dot{\epsilon}$ is nonlinear. The relation was shown in Fig. 7.

$$\log \sigma = a + b \log \dot{\epsilon} + c (\log \dot{\epsilon})^2 + d (\log \dot{\epsilon})^3 \quad (12)$$

The strain-rate-sensitivity index is calculated by taking the logarithm of Equation (12), i.e.,

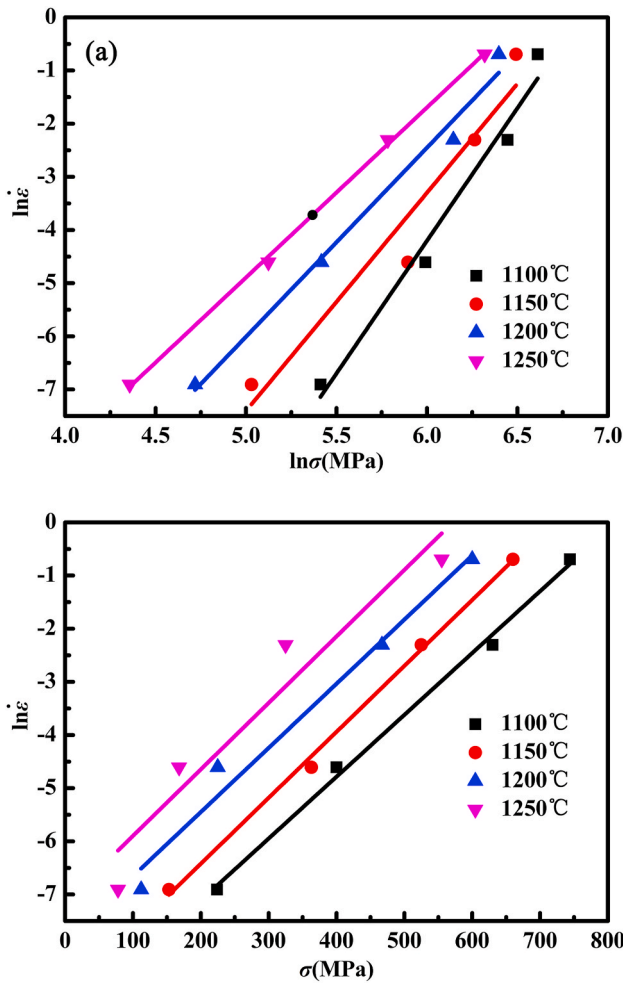


Fig. 4. Flow-stress analysis of the MoNbHfZrTi RHEA showing a linear fit for the (a) $\ln(\text{strain rate})$ vs. $\ln(\text{flow stress})$, and (b) $\ln(\text{strain rate})$ vs. flow stress.

$$m = \frac{d(\log \sigma)}{d(\log \dot{\epsilon})} = b + 2c \log \dot{\epsilon} + 3d(\log \dot{\epsilon})^2 \quad (13)$$

With the calculated m as used in Eqs. (10) and (11), the power dissipation factor, η , and the instability parameter, ξ , were acquired. A power-dissipation map and the instability map were drawn according to the obtained η and ξ values. Superposition of the power dissipation map and the instability map ultimately produce the hot-processing map of the material, as Fig. 8 gives. The hot-processing map is a graph to characterize the inherent processability of a material, and can be used to select appropriate deformation parameters to improve the processability of materials. The hot-processing map can also be used to control microstructures, study deformation mechanisms, and analyze the cause of plastic instability during deformation processes.

In the hot-processing map of the MoNbHfZrTi RHEA, the contour indicates the power-dissipation factor, while the shaded portion is the instability zone (Fig. 8). The only one instability region appears at 1100–1220 °C and $10^{-1.5} - 0.5 \text{ s}^{-1}$. The corresponding power-dissipation factor, η , in the instability region is the lowest with values ranging from 0.15 to 0.27. In the stable region, the power dissipation, η , increases with increasing temperatures or decreasing strain rates. The hot-processing map shows that the maximum power-dissipation efficiency takes place at 1110–1170 °C and $10^{-3} - 10^{-2.5} \text{ s}^{-1}$. To verify the hot-processing map, Fig. 9 shows the cracking map of the hot-deformed specimens at different processing parameters. The occurrence of cracks is essentially consistent with the instability zone indicated in Fig. 8.

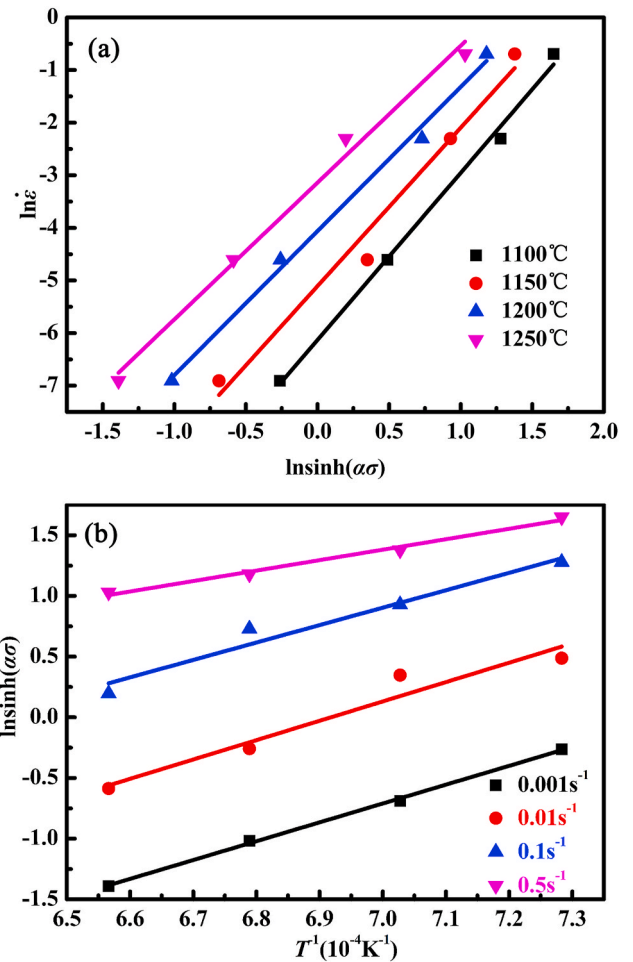


Fig. 5. Flow-stress analysis of the MoNbHfZrTi RHEA showing a linear fit for the (a) $\ln(\text{strain rate})$ vs. $\ln \sinh(\alpha\sigma)$, and (b) $\ln \sinh(\alpha\sigma)$ vs. $1/T$.

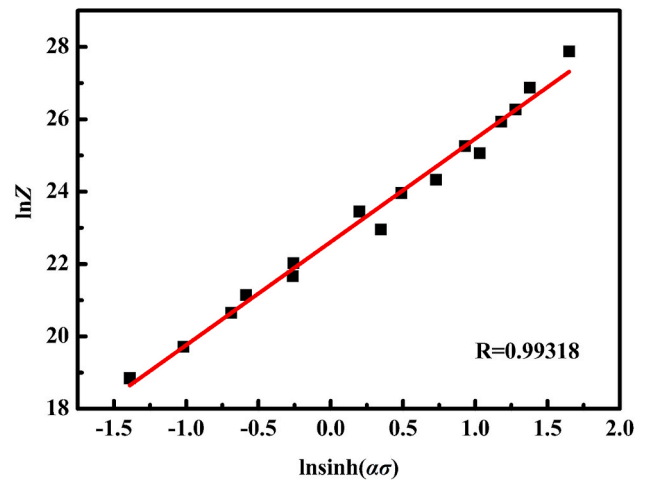


Fig. 6. Relationship between σ and Z .

3.5. Microstructures evolution of dynamic recrystallization

The microstructures after hot compression under different processing conditions were observed by EBSD. For all samples, observations were made in the uniformly-deformed central region. Inverse pole figure (IPF) maps and grain-boundary (GB) maps of the MoNbHfZrTi RHEA under different temperatures and strain rates indicate necklace-like

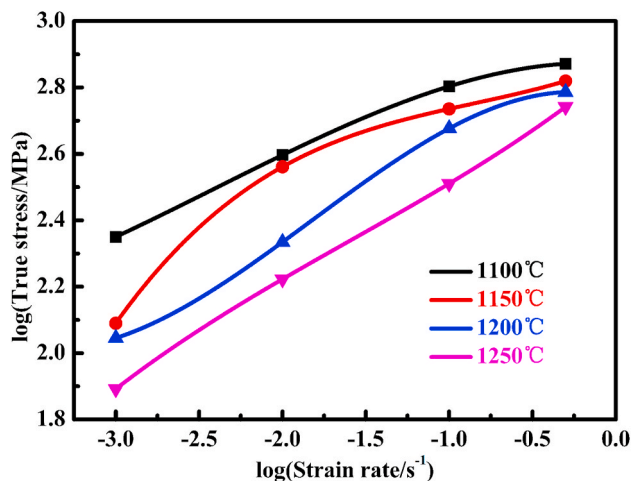


Fig. 7. Cubic linear fit for the log(flow stress) vs. log(strain rate).

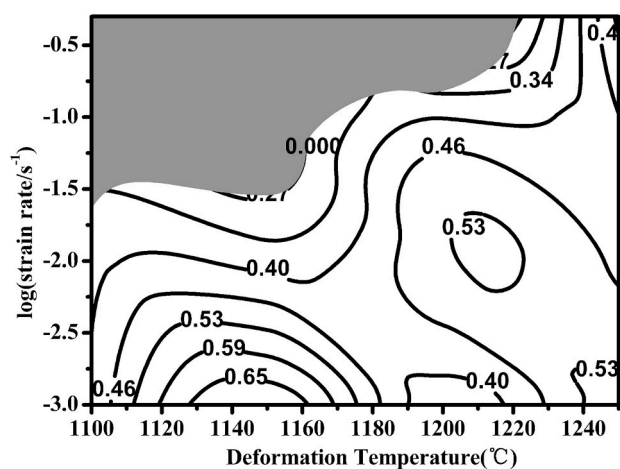


Fig. 8. The processing maps for the MoNbHfZrTi RHEA. The Grey part is the instability zone.

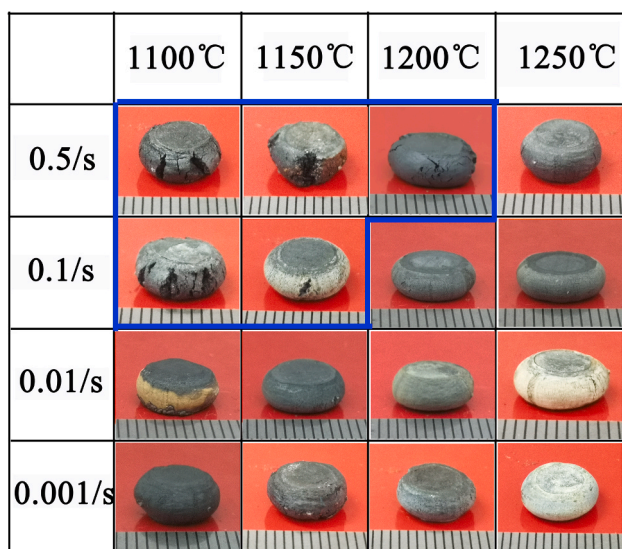


Fig. 9. The distribution of the cracking situation of the compressive specimens in hot deformation at a series of processing parameters, the instability zone is in blue. (For interpretation of the references to colour in this figure legend, the reader is referred to the Web version of this article.)

structures perpendicular to the compression axis (Fig. 10). In the GB maps, low-angle grain boundaries (2–5°) are in blue, intermediate-angle grain boundaries (5–15°) are in yellow, and high-angle grain boundaries (>15°) are in red. Under most conditions, fine and equiaxed grains appearing as original grain boundaries compose necklace-like structures, which are usually found in many face-centered-cubic (FCC) alloys [48,49]. These fine, equiaxed and undistorted grains are considered to be recrystallized grains, as also reported in other types of metals [50, 51]. Both the average size and proportion of the DRX grains increase with increasing deformation temperatures or decreasing strain rates. The test temperatures and strain rates are introduced into Eq. (7), and the relationship is expressed by the Z parameter, as given by Fig. 11.

At the same time, many high-angle grain boundaries (HAGBs) were found in the grain boundary and shear zone, and the formation of HAGBs is related to DRX [26,52]. Grain boundaries contribute greatly to the strength and toughness of the alloy. Thus, the formation of numerous HAGBs is very advantageous [53]. As shown in Fig. 10, in the region without DRX, a large number of low-angle grain boundaries and intermediate-angle grain boundaries are found, and there are many HAGBs in the DRX region, which indicates a gradual conversion from a low-angle grain boundary to HAGBs. These observations confirm the occurrence of the discontinuous dynamic recrystallization (DDRX). This type dynamic recrystallization, which has clear nucleation and growth stages, can be classified as a discontinuous process [54]. The formation of a necklace-like structure composed of fine recrystallized grains along the initial grain boundaries suggests that DDRX is active. Further enhanced DDRX can also be found at 1250 °C and 10⁻² s⁻¹ (Fig. 10g and h), indicating that the contribution of DDRX increases significantly, as Z decreases.

The microstructural evolution under various processing conditions was discussed before. To better study the relationship among the stress, dislocation, and DRX, local misorientation images were produced. The local EBSD misorientation image is considered to be a good indicator of the degree of work hardening, as shown in Fig. 12. It illustrates the degree of work hardening of the MoNbHfZrTi RHEA at different conditions. The degree of work hardening is negatively correlated with the distribution of DRX. In other words, the work hardening is high in the non-DRX region, while the dislocation density is low in the DRX region. The dislocation density decreases as the parameter, Z, decreases and DRX increases. It is showed here that the formation and growth of fine undistorted grains require the consumption of the dislocations, which offsets the dislocation stagnation. And the HAGBs can continue to migrate, eventually leading to softening with increasing the deformation temperatures or decreasing the strain rates.

4. Discussions

The average size and proportion of the DRX grains increase, respectively from 1.8 to 5 μm and from 0.35 to 0.82, respectively, as the Z parameter decreases (Fig. 11). At 1100 °C and 0.5s⁻¹(Fig. 10a and b), necklace-like structures with fine undistorted grains (1.8 μm) were observed along the original grain boundaries. The fraction of the DRX grains is relatively low (0.35), where hard working is dominant. At 1100 °C and 0.1 s⁻¹ (Fig. 10c and d), necklace-like structures with fine undistorted grains (2.2 μm) were observed along the shear-deformation region, the fraction of the DRX grains is 0.42. The size and fraction of the DRX grains tend to increase (from 3 μm, 0.53–5 μm, 0.82) with the change of deformation conditions from 1100 °C to 0.01s⁻¹(Fig. 10e and f) to 1250 °C and 0.01s⁻¹(Fig. 10g and h), respectively, where stress is low. Both the fractions of DRX grains and size increase with increasing the deformation temperature and decreasing the strain rate. The increased deformation temperature will promote the development of DRX grains during deformation, and the increased deformation temperature can also accelerate the migration rate of dynamically-recrystallized grain boundaries, and the high-deformation temperature can supply more thermal activation energy for the development of DRX

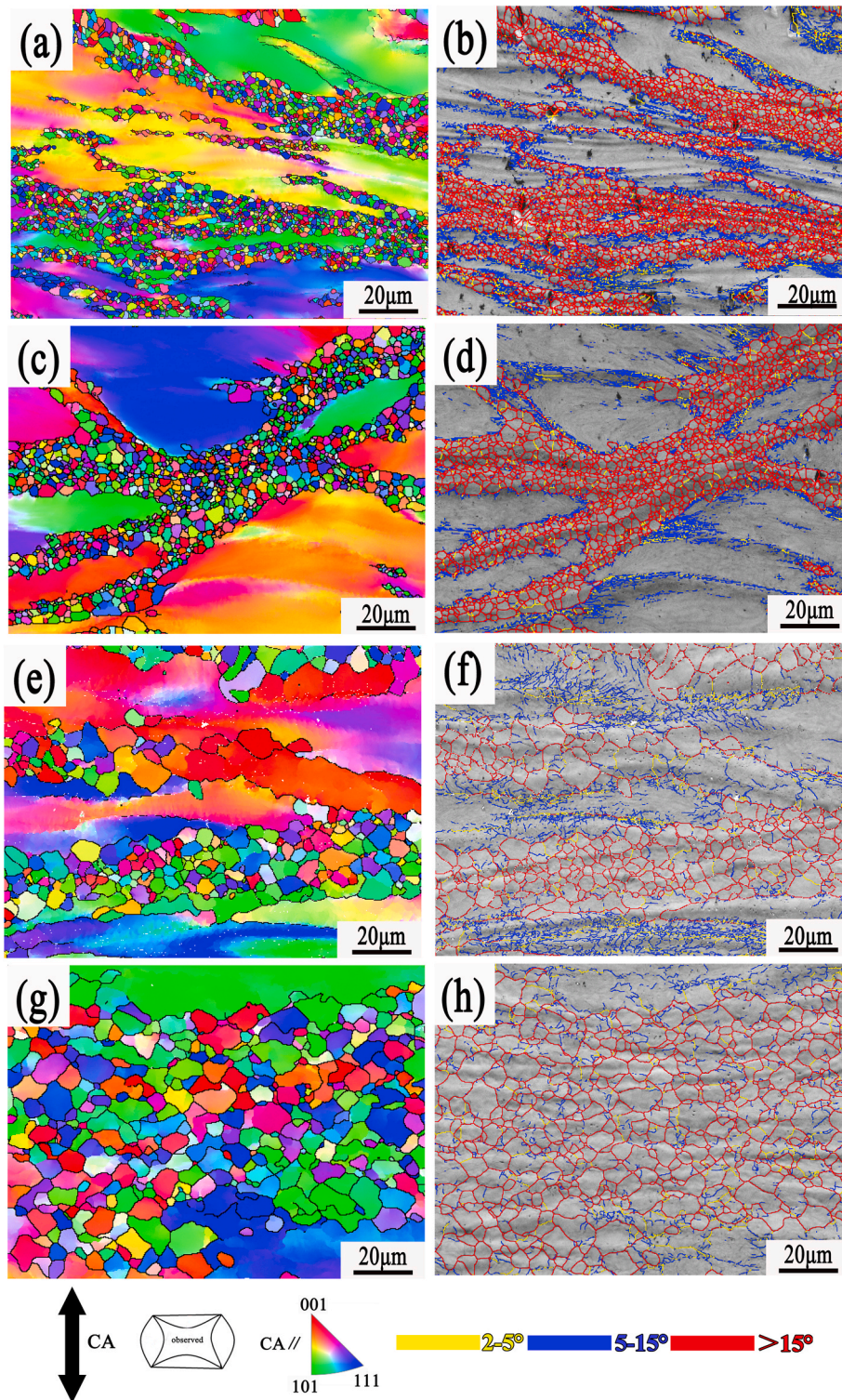


Fig. 10. The IPF and GB maps of the microstructures of the MoNbHfZrTi RHEA after hot deformation under different processing conditions. IPF and GB: (a) (b) 1100 °C 0.5s⁻¹; (c) (d) 1100 °C 0.1s⁻¹; (e) (f) 1100 °C 0.01s⁻¹; (g) (h) 1250 °C 0.01s⁻¹. In the GB maps, low-angle grain boundaries (2–5°) are in blue, intermediate-angle grain boundaries (5–15°) are in yellow, and high-angle grain boundaries (>15°) are in red. (For interpretation of the references to colour in this figure legend, the reader is referred to the Web version of this article.)

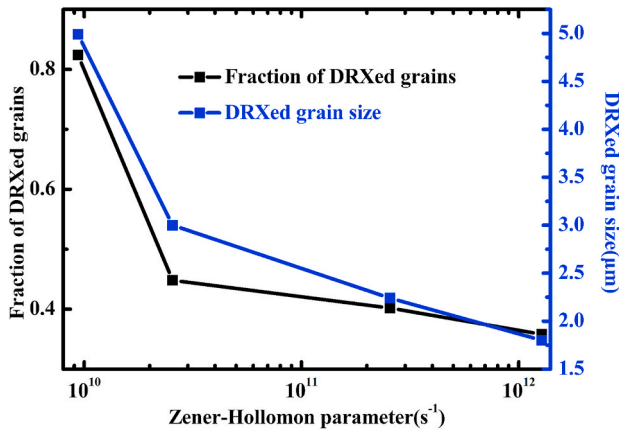


Fig. 11. Relationship among the size of DRXed grains, the fraction of DRXed grains, and the parameter, Z .

grains. Decreased strain rate offers sufficient time for the dislocation motion, grain-boundary migration, and finally the grains grew and strength softened.

Combined with the above microstructures, Fig. 10a and c are in the instability zone, while Fig. 10e and g are in the well-processed zone. In the instability zone, the average DRX grains are fine, the DRX fraction is small, and the corresponding Z parameter is high. The DRX grains are found along the shear-deformation region (Fig. 10c and d). While in the well-processed zone, the average DRX grains are large, the DRX fraction is large, and the corresponding parameter Z is low. That is to say, to better process the material and consider the processing cost, processing should be carried out under the condition at 1110–1170 °C and 10^{-3} - $10^{-2.5}$ s^{-1} . In other words, in the region, the highest fraction of the deformation energy applied is used for the microstructural development.

5. Conclusions

Hot-deformation mechanisms, flow-stress analysis, and processing maps of the equiatomic MoNbHfZrTi refractory high-entropy alloy were studied by hot-compression testing temperatures ranging from 1100 to 1250 °C and strain rates varying from 10^{-3} to $0.5 s^{-1}$, from which the following conclusions are derived as.

- (1) The stress first increases and then decreases constantly with increasing the strain which is a typical sign of dynamic recrystallization (DRX) in hot-deformation samples. The peak stress decreases with increasing the deformation temperature and decreasing the strain rate.
- (2) The relationships among the temperature (T), strain rate ($\dot{\epsilon}$) and stress (σ) were studied. The apparent activation energy (Q) was determined to be 326.1 kJ/mol. A constitutive equation of the MoNbHfZrTi refractory high-entropy alloy is

$$\dot{\epsilon} = 6.60 \times 10^9 [\sinh(0.00316\sigma)]^{2.88232} \exp\left(\frac{-326.111}{RT}\right)$$

- (3) According to hot-processing maps, the dissipation, η , increases with increasing the deformation temperature or decreasing the strain rate. There is only one instability region at 1100–1220 °C and $10^{-1.5}$ - $0.5 s^{-1}$, and the optimal processing area is determined at the deformation temperature of 1110–1170 °C and strain rate of 10^{-3} - $10^{-2.5} s^{-1}$.
- (4) Stress-strain curves indicated the characteristic-softening behavior due to DRX. The formation and growth of fine undistorted grains require the consumption of the accumulated dislocations, which offsets the dislocation stagnation and stress of the material drop. Fine and undistorted grains appearing at initial grain boundaries and shear bands form necklace-like structures. A gradual conversion from a low-angle grain boundary to HAGBs was found, indicating that the contribution of DDRX increases significantly as Z decreases.

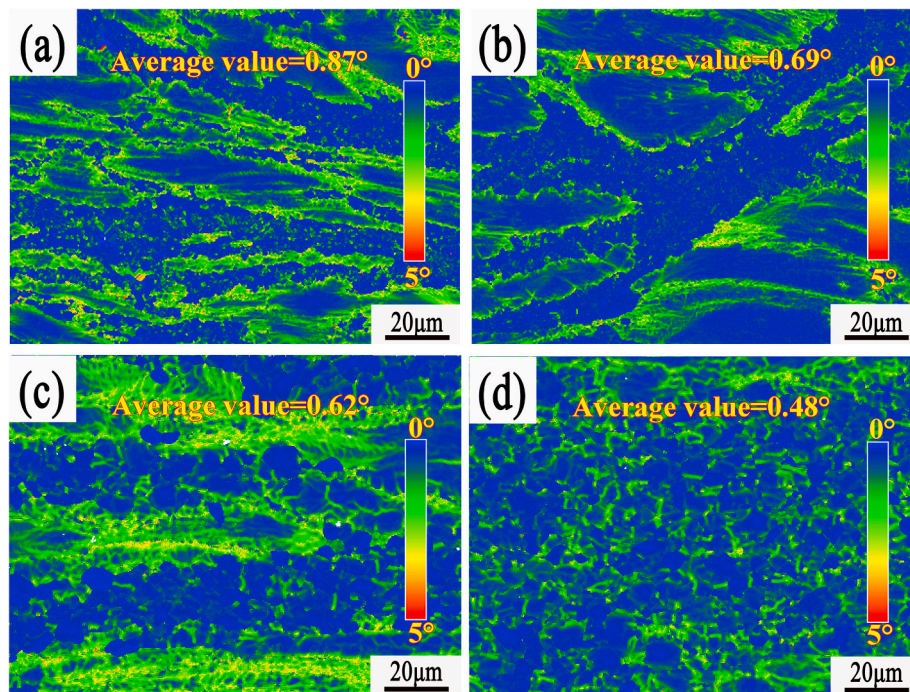


Fig. 12. Local misorientation maps of the MoNbHfZrTi RHEA after hot deformation under different processing conditions: (a) 1100 °C $0.5s^{-1}$; (b) 1100 °C $0.1s^{-1}$; (c) 1100 °C $0.01s^{-1}$; (d) 1250 °C $0.01s^{-1}$.

- (5) Both the proportion of fine undistorted grains and the average grain size increase with increasing the deformation temperature or decreasing the strain rate. In other words, the average size and fraction of DRX grains increase from 1.8 to 5 μm and from 0.35 to 0.82, respectively, as the parameter, Z , decreases. In the instability zone, the DRX grains along the shear-deformation region were observed, which might have been the crack-initiation zone. The fraction of DRX grains and the average size are low in the instability zone, but are relatively high in the well-processed zone.

Author statement

The work described has not been submitted elsewhere for publication, in whole or in part, and all authors listed have approved the enclosed manuscript. Fuyu Dong and Yue Zhang designed experiments. Ye Yuan carried out experiments. Yue Zhang, Weidong Li, P.K. Liaw, Xiaoguang Yuan, Hongjun Huang analyzed experimental results. Fuyu Dong and Ye Yuan wrote the manuscript.

Declaration of competing interest

The authors declare that they have no known competing financial interests or personal relationships that could have appeared to influence the work reported in this paper.

Acknowledgments

The present work was supported by (1) the Natural Science Foundation of Liaoning Province (20180510056 and 2019-ZD-0216), (2) the Foundation of Liaoning Province Education Administration (LQGD2019001), and (3) the National Natural Science Foundation of China (51401129). PKL thanks the support from (1) the National Science Foundation Programs (DMR-1611180 and 1809640) with the program directors, Drs. G. Shiflet and D. Farkas and (2) from the U.S. Army Office Projects (W911NF-13-1-0438 and W911NF-19-2-0049) with the program managers, Drs. M. P. Bakas, D. M. Stepp, and S. Mathaudhu.

References

- [1] B. Cantor, I.T.H. Chang, P. Knight, A.J.B. Vincent, Microstructural development in equiatomic multicomponent alloys, *Mater. Sci. Eng., A* 375 (2004) 213–218.
- [2] J. Yeh, S. Chen, S. Lin, J. Gan, T. Chin, T. Shun, C. Tsau, S. Chang, Nanostructured high-entropy alloys with multiple principal elements: novel alloy design concepts and outcomes, *Adv. Eng. Mater.* 6 (2004) 299–303.
- [3] Y. Zhang, T.T. Zuo, Z. Tang, M.C. Gao, K.A. Dahmen, P.K. Liaw, Z.P. Lu, Microstructures and properties of high-entropy alloys, *Prog. Mater. Sci.* 61 (2014) 1–93.
- [4] D.B. Miracle, O.N. Senkov, A critical review of high entropy alloys (HEAs) and related concepts, *Acta Mater.* 122 (2017) 448–511.
- [5] G. Liu, D.H. Lu, X.W. Liu, F.C. Liu, Q. Yang, H. Du, Q. Hu, Z.T. Fan, Solute segregation effect on grain boundary migration and Hall-Petch relationship in CrMnFeCoNi high-entropy alloy, *Mater. Sci. Technol.* (2019) 1–9.
- [6] Y. Lu, Y. Dong, S. Guo, L. Jiang, H. Kang, T. Wang, B. Wen, Z. Wang, J. Jie, Z. Cao, A promising new class of high-temperature alloys: eutectic high-entropy alloys, *Sci. Rep.* 4 (2015) 6200, 6200.
- [7] P. Shi, W. Ren, T. Zheng, Z. Ren, X. Hou, J. Peng, P. Hu, Y. Gao, Y. Zhong, P. K. Liaw, Enhanced strength-ductility synergy in ultrafine-grained eutectic high-entropy alloys by inheriting microstructural lamellae, *Nat. Commun.* 10 (2019) 489.
- [8] O.N. Senkov, G.B. Wilks, D.B. Miracle, C. Chuang, P.K. Liaw, Refractory high-entropy alloys, *Intermetallics* 18 (2010) 1758–1765.
- [9] K.M. Youssef, A.J. Zaddach, C. Niu, D.L. Irving, C.C. Koch, A novel low-density, high-hardness, high-entropy alloy with close-packed single-phase nanocrystalline structures, *Mater. Res. Lett.* 3 (2015) 95–99.
- [10] R. Feng, M.C. Gao, C. Lee, M. Mathes, T. Zuo, S. Chen, J.A. Hawk, Y. Zhang, P. K. Liaw, Design of light-weight high-entropy alloys, *Entropy* 18 (2016) 333.
- [11] R. Feng, M.C. Gao, C. Zhang, W. Guo, J.D. Poplawsky, F. Zhang, J.A. Hawk, J. C. Neufeld, Y. Ren, P.K. Liaw, Phase stability and transformation in a light-weight high-entropy alloy, *Acta Mater.* 146 (2018) 280–293.
- [12] Y. Cao, Y. Liu, Y. Li, B. Liu, J. Wang, M. Du, R. Liu, Precipitation strengthening in a hot-worked TiNbTa_{0.5}ZrAl_{0.5} refractory high entropy alloy, *Mater. Lett.* 246 (2019) 186–189.
- [13] T.M. Butler, K.J. Chaput, Native oxidation resistance of Al₂₀Nb₃₀Ta₁₀Ti₃₀Zr₁₀ refractory complex concentrated alloy (RCCA), *J. Alloys Compd.* 787 (2019) 606–617.
- [14] S. Alvi, F. Akhtar, High temperature tribology of CuMoTaWV high entropy alloy, *Wear* 426–427 (2019) 412–419.
- [15] H. Song, F. Tian, D. Wang, Thermodynamic properties of refractory high entropy alloys, *J. Alloys Compd.* 682 (2016) 773–777.
- [16] Y. Zou, S. Maiti, W. Steurer, R. Spolenak, Size-dependent plasticity in an Nb₂₅Mo₂₅Ta₂₅W₂₅ refractory high-entropy alloy, *Acta Mater.* 65 (2014) 85–97.
- [17] C. Juan, M. Tsai, C. Tsai, C.Y. Lin, W. Wang, C. Yang, S. Chen, S. Lin, J. Yeh, Enhanced mechanical properties of HfMoTaTiZr and HfMoNbTaTiZr refractory high-entropy alloys, *Intermetallics* 62 (2015) 76–83.
- [18] Y. Wu, J.J. Si, D. Lin, T. Wang, W.Y. Wang, Y. Wang, Z. Liu, X. Hui, Phase stability and mechanical properties of AlHfNbTiZr high-entropy alloys, *Mater. Sci. Eng., A* 724 (2018) 249–259.
- [19] D. Liu, P.F. Yu, G. Li, P.K. Liaw, R.P. Liu, High-temperature high-entropy alloys Al₃Co₁₅Cr₁₅Ni₇₀, based on the Al-Ni binary system, *Mater. Sci. Eng., A* 724 (2018) 283–288.
- [20] N.Y. Yurchenko, N.D. Stepanov, S.V. Zherebtsov, M.A. Tikhonovskiy, G. A. Salishchev, Structure and mechanical properties of B2 ordered refractory AlNbTiVZr_x (x=0–1.5) high-entropy alloys, *Mater. Sci. Eng., A* 704 (2017) 82–90.
- [21] A. Shafiee, J. Moon, H.S. Kim, M. Jahazi, M. Nili Ahmadabadi, Precipitation behaviour and mechanical properties of a new wrought high entropy superalloy, *Mater. Sci. Eng., A* 749 (2019) 271–280.
- [22] D.B. Miracle, O.N. Senkov, J.M. Scott, G.B. Wilks, Mechanical properties of Nb₂₅Mo₂₅Ta₂₅W₂₅ and V₂₀Nb₂₀Mo₂₀Ta₂₀W₂₀ refractory high entropy alloys, *Intermetallics* 19 (2011) 698–706.
- [23] O.N. Senkov, S.L. Semiatin, Microstructure and properties of a refractory high-entropy alloy after cold working, *J. Alloys Compd.* 649 (2015) 1110–1123.
- [24] N.N. Guo, L. Wang, L.S. Luo, X.Z. Li, Y.Q. Su, J.J. Guo, H.Z. Fu, Microstructure and mechanical properties of refractory MoNbHfZrTi high-entropy alloy, *Mater. Des.* 81 (2015) 87–94.
- [25] S. Praveen, H.S. Kim, High-entropy alloys: potential candidates for high-temperature applications - an overview, *Adv. Eng. Mater.* 20 (2018) 1700645.
- [26] Y. Wang, J. Li, Y. Xin, C. Li, Y. Cheng, X. Chen, M. Rashad, B. Liu, Y. Liu, Effect of Zener-Hollomon parameter on hot deformation behavior of CoCrFeMnNiCo_{0.5} high entropy alloy, *Mater. Sci. Eng., A* 768 (2019) 138483.
- [27] X. Wang, Y. Zhang, X. Ma, High temperature deformation and dynamic recrystallization behavior of AlCrCuFeNi high entropy alloy, *Mater. Sci. Eng., A* 778 (2020) 139077.
- [28] M. Patnamsetty, A. Saastamoinen, M.C. Somani, P. Peura, Constitutive modelling of hot deformation behaviour of a CoCrFeMnNi high-entropy alloy, *Sci. Technol. Adv. Mater.* 21 (2020) 43–55.
- [29] W. Kim, H.T. Jeong, H.K. Park, K. Park, T. Na, E. Choi, The effect of Al to high-temperature deformation mechanisms and processing maps of Al_{0.5}CoCrFeMnNi high entropy alloy, *J. Alloys Compd.* 802 (2019) 152–165.
- [30] Y.T. Wang, J.B. Li, Y.C. Xin, X.H. Chen, M. Rashad, B. Liu, Y. Liu, Hot deformation behavior and hardness of a CoCrFeMnNi high-entropy alloy with high content of carbon, *Acta Metall. Sin.* 32 (2019) 932–943.
- [31] N.N. Guo, L. Wang, L.S. Luo, X.Z. Li, R.R. Chen, Y.Q. Su, J.J. Guo, H.Z. Fu, Hot deformation characteristics and dynamic recrystallization of the MoNbHfZrTi refractory high-entropy alloy, *Mater. Sci. Eng., A* 651 (2016) 698–707.
- [32] R.R. Eleti, T. Bhattacharjee, A. Shibata, N. Tsuji, Unique deformation behavior and microstructure evolution in high temperature processing of HfNbTaTiZr refractory high entropy alloy, *Acta Mater.* 171 (2019) 132–145.
- [33] N. Prasad, N. Bibhanshu, N. Nayan, G.S. Avadhani, S. Suwas, Hot deformation behavior of the high-entropy alloy CoCuFeMnNi, *J. Mater. Res.* 34 (2019) 744–755.
- [34] H.T. Jeong, H.K. Park, K. Park, T. Na, W. Kim, High-temperature deformation mechanisms and processing maps of equiatomic CoCrFeMnNi high-entropy alloy, *Mater. Sci. Eng., A* 756 (2019) 528–537.
- [35] R. Jain, M.R. Rahul, S. Samal, V. Kumar, G. Phanikumar, Hot workability of Co-Fe-Mn-Ni-Ti eutectic high entropy alloy, *J. Alloys Compd.* 822 (2020) 9.
- [36] K. Huang, R.E. Loge, A review of dynamic recrystallization phenomena in metallic materials, *Mater. Des.* 111 (2016) 548–574.
- [37] X. Chen, Y.C. Lin, D. Wen, J. Zhang, M. He, Dynamic recrystallization behavior of a typical nickel-based superalloy during hot deformation, *Mater. Des.* 57 (2014) 568–577.
- [38] A. Nicolay, G. Fiorucci, J.P.M. Franchet, J. Cormier, N. Bozzolo, Influence of strain rate on subsolvus dynamic and post-dynamic recrystallization kinetics of Inconel 718, *Acta Mater.* 174 (2019) 406–417.
- [39] S.L. Yu, Y. Gao, C.M. Liu, H.C. Xiao, Dynamic recrystallization behavior of Mg-Gd-Y-Zr alloy during hot compression, *Mater. Sci. Forum* 849 (2016) 181–185.
- [40] G. He, Y. Zhao, B. Gan, X. Sheng, Y. Liu, L. Tan, Mechanism of grain refinement in an equiatomic medium-entropy alloy CrCoNi during hot deformation, *J. Alloys Compd.* 815 (2020) 152382.
- [41] C.M. Sellars, W.J. McGearty, On the mechanism of hot deformation, *Acta Metall.* 14 (1966) 1136–1138.
- [42] C. Zener, J.H. Hollomon, Effect of strain rate upon plastic flow of steel, *J. Appl. Phys.* 15 (1944) 22–32.
- [43] Y.V.R.K. Prasad, H.L. Gegel, S.M. Doraivelu, J.C. Malas, J.T. Morgan, K.A. Lark, D. R. Barker, Modeling of dynamic material behavior in hot deformation: forging of Ti-6242, *Metall. Mater. Trans. Phys. Metall. Mater. Sci.* 15 (1984) 1883–1892.
- [44] R. Raj, Development of a processing map for use in warm-forming and hot-forming processes, *Metall. Mater. Trans. Phys. Metall. Mater. Sci.* 12 (1981) 1089–1097.

- [45] J. Zhang, H. Di, H. Wang, K. Mao, T. Ma, Y. Cao, Hot deformation behavior of Ti-15-3 titanium alloy: a study using processing maps, activation energy map, and Zener-Hollomon parameter map, *J. Mater. Sci.* 47 (2012) 4000–4011.
- [46] Y.V.R.K. Prasad, Processing maps: a status report, *J. Mater. Eng. Perform.* 12 (2003) 638–645.
- [47] Y.V.R.K. Prasad, Recent advances in the science of mechanical processing, *Indian J. Technol.* 28 (1990) 435–451.
- [48] N. Tsuji, Y. Matsubara, Y. Saito, Dynamic recrystallization of ferrite in interstitial free steel, *Scripta Mater.* 37 (1997) 477–484.
- [49] F.J. Humphreys, M. Hatherly, Chapter 13-Hot Deformation and Dynamic Restoration, Elsevier, Oxford, 2004.
- [50] C.K. Yan, A.H. Feng, S.J. Qu, G.J. Cao, J. Sun, J. Shen, D.L. Chen, Dynamic recrystallization of titanium: effect of pre-activated twinning at cryogenic temperature, *Acta Mater.* 154 (2018) 311–324.
- [51] S. Irukuvarghula, H. Hassanin, C. Cayron, M.M. Attallah, D. Stewart, M. Preuss, Evolution of grain boundary network topology in 316L austenitic stainless steel during powder hot isostatic pressing, *Acta Mater.* 133 (2017) 269–281.
- [52] P. Cizek, The microstructure evolution and softening processes during high-temperature deformation of a 21Cr-10Ni-3Mo duplex stainless steel, *Acta Mater.* 106 (2016) 129–143.
- [53] A. Belyakov, K. Tsuzaki, H. Miura, T. Sakai, Effect of initial microstructures on grain refinement in a stainless steel by large strain deformation, *Acta Mater.* 51 (2003) 847–861.
- [54] H. Jazaeri, F.J. Humphreys, The transition from discontinuous to continuous recrystallization in some aluminium alloys: II - annealing behaviour, *Acta Mater.* 52 (2004) 3251–3262.